

ARTICLE OPEN



648 Hilbert-space dimensionality in a biphoton frequency comb: entanglement of formation and Schmidt mode decomposition

Kai-Chi Chang^{1,6}, Xiang Cheng^{1,6}, Murat Can Sarihan¹, Abhinav Kumar Vinod¹, Yoo Seung Lee¹, Tian Zhong², Yan-Xiao Gong³, Zhenda Xie⁴, Jeffrey H. Shapiro⁵, Franco N. C. Wong⁵ and Chee Wei Wong¹

Qudit entanglement is an indispensable resource for quantum information processing since increasing dimensionality provides a pathway to higher capacity and increased noise resilience in quantum communications, and cluster-state quantum computations. In continuous-variable time–frequency entanglement, encoding multiple qubits per photon is only limited by the frequency correlation bandwidth and detection timing jitter. Here, we focus on the discrete-variable time–frequency entanglement in a biphoton frequency comb (BFC), generating by filtering the signal and idler outputs with a fiber Fabry–Pérot cavity with 45.32 GHz free-spectral range (FSR) and 1.56 GHz full-width-at-half-maximum (FWHM) from a continuous-wave (cw)-pumped type-II spontaneous parametric downconverter (SPDC). We generate a BFC whose time-binned/frequency-binned Hilbert space dimensionality is at least 324, based on the assumption of a pure state. Such BFC’s dimensionality doubles up to 648, after combining with its post-selected polarization entanglement, indicating a potential 6.28 bits/photon classical-information capacity. The BFC exhibits recurring Hong–Ou–Mandel (HOM) dips over 61 time bins with a maximum visibility of 98.4% without correction for accidental coincidences. In a post-selected measurement, it violates the Clauser–Horne–Shimony–Holt (CHSH) inequality for polarization entanglement by up to 18.5 standard deviations with an S -parameter of up to 2.771. It has Franson interference recurrences in 16 time bins with a maximum visibility of 96.1% without correction for accidental coincidences. From the zeroth- to the third-order Franson interference, we infer an entanglement of formation (E_{of}) up to 1.89 ± 0.03 ebits—where 2 ebits is the maximal entanglement for a 4×4 dimensional biphoton—as a lower bound on the 61 time-bin BFC’s high-dimensional entanglement. To further characterize time-binned/frequency-binned BFCs we obtain Schmidt mode decompositions of BFCs generated using cavities with 45.32, 15.15, and 5.03 GHz FSRs. These decompositions confirm the time–frequency scaling from Fourier-transform duality. Moreover, we present the theory of conjugate Franson interferometry—because it is characterized by the state’s joint-temporal intensity (JTI)—which can further help to distinguish between pure-state BFC and mixed state entangled frequency pairs, although the experimental implementation is challenging and not yet available. In summary, our BFC serves as a platform for high-dimensional quantum information processing and high-dimensional quantum key distribution (QKD).

npj Quantum Information (2021)7:48; <https://doi.org/10.1038/s41534-021-00388-0>

INTRODUCTION

Qudit entanglement is a fundamental differentiator of quantum information processing over classical systems in computing, communications, simulations, and metrology. The dimensionality and information capacity encoded in entanglement scales with both the number of physical qudits in multipartite systems and the dimensionality of each qudit^{1–11}. Entanglement between multi-dimensional quantum systems (e.g., the mode structure of two-photon states of light)^{12–21} can be addressed in spatial-temporal energy properties such as orbital angular momentum^{22,23}, position-momentum^{24–29}, polarization^{30,31}, energy–time^{32–34}, and time–frequency^{35–44}, and it has applications that include d -dimensional cluster-state quantum computation^{11,38,45} and spectral-shearing interferometry⁴⁰. In quantum communications, such as device-independent quantum cryptography, high dimensionality provides a pathway toward increased information capacity per photon^{12,20,34,45–50}, improved security against various

attacks⁵¹, and better resilience against noise and errors^{52,53}. Consequently, advances in high-dimensional qudit encoding have ranged from Bell-type inequalities for energy–time qudits^{22,35,54,55}, to on-chip quantum frequency-comb generation^{36,56}, to certifying high-dimensional entanglement via two global product bases without requiring full state tomography⁵⁷. The dimensionality of such qudits include: compressive sensing of joint quantum systems with 65,536 dimensions in the position-momentum degrees-of-freedom²⁴, on-chip frequency-bin generation with at least 100 dimensions³⁶; and 19 time-bin qubits in BFCs³⁵, scaling remarkably to 84 time-bin revivals with a path length difference of 100 m⁵⁸. Recently, this record has been extended drastically up to encoding the equivalent of 20 qubits using only biphotons to create multipartite GHZ states⁴². To date, however, the Hilbert space dimensionality of time–frequency entanglement has always been less than 100 in BFCs generated with fiber cavity filtering of a continuous-wave (cw)-pumped SPDC source, and the complete

¹Fang Lu Mesoscopic Optics and Quantum Electronics Laboratory, Department of Electrical and Computer Engineering & Center for Quantum Science and Engineering, University of California, Los Angeles, CA, USA. ²Institute for Molecular Engineering, University of Chicago, Chicago, IL, USA. ³National Laboratory of Solid State Microstructures and School of Physics, Nanjing University, Nanjing 210093, PR China. ⁴National Laboratory of Solid State Microstructures and School of Electronic Science and Engineering, Nanjing University, Nanjing 210093, PR China. ⁵Research Laboratory of Electronics, Massachusetts Institute of Technology, Cambridge, MA, USA. ⁶These authors contributed equally: Kai-Chi Chang, Xiang Cheng. ✉email: uclakcchang@ucla.edu; chengxiang@ucla.edu; xiezhennda@nju.edu.cn; cheewei.wong@ucla.edu

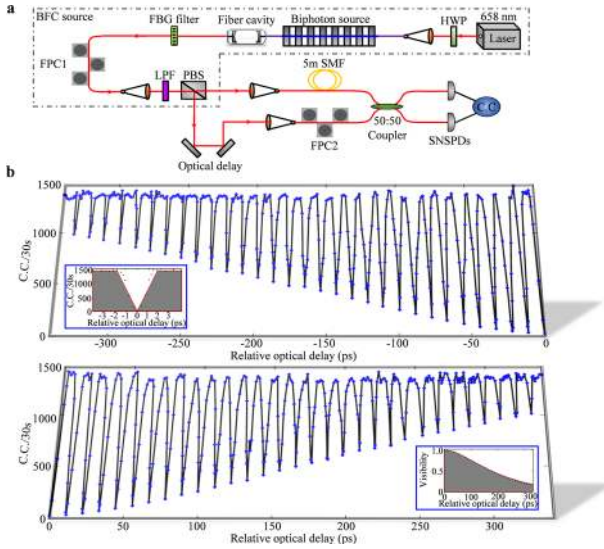


Fig. 1 High-dimensional BFC generation and HOM recurrence observation. **a** Illustrative experimental configuration. HWP half-wave plate, FBG fiber Bragg grating, FPC fiber polarization controller, LPF long-pass filter, PBS polarizing beam splitter, SNSPDs superconducting nanowire single-photon detectors, C.C. coincidence counts. **b** Coincidence counts versus relative optical delay from -340 to $+340$ ps, between the two arms of the HOM interferometer. HOM-interference recurrences are observed with up to 61 time bins. Upper left inset: zoom-in of the coincidence counts around zero relative delay between the two arms of the HOM interferometer. The dip width was fit to 3.86 ± 0.30 ps, which matches well with the reciprocal of the 245 GHz phase-matching bandwidth, as predicted by theory. The central dip visibility is 98.4% before and 99.9% after subtracting accidental coincidences. Lower right inset: measured time-bin visibilities versus the HOM optical delay compared with theory (red solid line, details in Supplementary Discussion I).

Schmidt mode decomposition of such time–frequency qudits has yet to be fully explored.

Here we report a BFC generated by filtering the signal and idler outputs from a cw-pumped, type-II quasi-phase-matched (245 GHz FWHM phase-matching bandwidth), frequency-degenerate SPDC source using a fiber Fabry–Pérot cavity with 45.32 GHz FSR and 1.56 GHz FWHM linewidth. This BFC’s time-binned/frequency-binned Hilbert space dimensionality is at least 324, based on the assumption that our BFC is a pure state. Moreover, when combined with its post-selected polarization entanglement, the BFC’s dimensionality doubles to at least 648, implying it has a 6.28 bits/photon classical-information capacity. We characterized this BFC in a variety of ways. First, we observed 61 periodic revivals of Hong–Ou–Mandel (HOM) interference with visibility up to 98.4% without correction for accidental coincidences⁵⁹. Second, we demonstrated this BFC’s spectral correlations across five frequency bins. Next, by switching to a BFC produced with the same SPDC source and a 5.03 GHz FSR, 0.46 GHz FWHM linewidth cavity, we got spectral correlations over 19 frequency bins but only seven HOM-interference recurrences. This result is in keeping with the scaling associated with Fourier-transform duality, i.e., more time bins imply fewer frequency bins and vice versa. In additional tests of the 45.32-GHz-cavity source we first did a post-selected measurement that violated the Clauser–Horne–Shimony–Holt (CHSH) inequality for polarization entanglement by up to 18.5 standard deviations with an S -parameter of up to 2.771. Then we witnessed Franson interference recurrences in 16 time bins with a maximum visibility of 96.1% without correction for accidental coincidences. From the zeroth- to third-order Franson interference, we inferred an entanglement of formation (E_{or}) up to 1.89 ± 0.03 ebits—where

two ebits is the maximal entanglement for a 4×4 dimensional biphoton—as a lower bound on the 61 time-bin BFC’s high-dimensional entanglement. To further characterize time-binned/frequency-binned BFCs we performed Schmidt mode decompositions of BFCs generated using cavities our three (45.32, 15.15, and 5.03 GHz FSR) cavities. These decompositions confirm the time–frequency scaling from Fourier-transform duality that was seen earlier in our spectral correlations and HOM-interference recurrences. For the 45.32 GHz cavity, the resulting Hilbert space dimensionality of the time-binned/frequency-binned BFC was at least 324. Augmented by this state’s post-selected polarization entanglement, this state’s dimensionality doubles to at least 648, which represents an $\approx 7.5 \times$ improvement over our prior studies³⁵ and is equivalent to a more than 13 qubit computational space that can encode 6.28 bits/photon classical-information capacity in a biphoton-based communication link.

Although standard perturbation theory predicts that our BFC-generation procedure produces high-purity states, we further describe the theoretical analysis and modeling from conjugate Franson interferometry. Characterized by the state’s joint-temporal intensity (JTI), it can help to directly distinguish between the desired pure-state BFC and a mixed state of entangled frequency pairs (which has the same joint spectral intensity), although the experimental implementation is challenging and not yet available. In summary, our 13 qubit high-dimensional BFC can serve as a platform for hybrid time–frequency quantum key distribution (QKD), time–frequency cluster-state quantum computation, and high-dimensional encoding in quantum networks.

RESULTS

HOM dip recurrences

Our experimental setup is illustrated in Fig. 1a. The SPDC source used a type-II quasi-phase-matched, periodically-poled KTiOPO_4 (ppKTP) waveguide, integrated in a fiber package for high fluence and efficiency⁶⁰. It was pumped by a 658 nm wavelength Fabry–Pérot laser diode, stabilized by self-injection locking. Our SPDC entangled photon source was designed to generate orthogonally-polarized, frequency-degenerate signal-idler photon pairs at 1316 nm with 245 GHz FWHM phase-matching bandwidth⁶¹. Three high-dimensional BFCs³⁵ were created by sending the signal-idler photon pairs through one of three Fabry–Pérot fiber cavities, whose FSRs are 45.32, 15.15, and 5.03 GHz, with FWHM linewidths of 1.56, 1.36, and 0.46 GHz, respectively. Each fiber cavity was mounted on a modified thermoelectric assembly with ≈ 1 mK temperature-control stability. A stabilized tunable reference laser at 1316 nm was used to align each cavity’s spectrum to the SPDC’s degenerate frequency. The resulting BFC biphoton—as predicted by standard perturbation theory with the signal-idler differential group delay suppressed, see for example⁶²—can be expressed as:

$$|\psi\rangle = \sum_{m=-N_0}^{N_0} \int d\Omega f'(\Omega) f(\Omega - m\Delta\Omega) \hat{a}_H^\dagger\left(\frac{\omega_p}{2} + \Omega\right) \hat{a}_V^\dagger\left(\frac{\omega_p}{2} - \Omega\right) |0\rangle. \quad (1)$$

Here: \hat{a}_H^\dagger and \hat{a}_V^\dagger are creation operators for horizontally and vertically polarized photons; $\Delta\Omega$ is the cavity FSR in rad s^{-1} ; Ω is the detuning of the SPDC’s biphotons from frequency degeneracy; $2N_0 + 1$ is the number of cavity lines passed by an overall bandwidth-limiting filter; $f'(\Omega) = \text{sinc}(A\Omega)$ is the SPDC source’s phase-matching function, where $A = 2.78/\pi B_{\text{PM}}$ with B_{PM} being the FWHM bandwidth; and $f(\Omega - m\Delta\Omega)$ is the single frequency-bin profile defined by the cavity’s Lorentzian transmission

lineshape with FWHM linewidth $2\Delta\omega$, viz.,

$$f(\Omega) = \frac{1}{[(\Delta\omega)^2 + \Omega^2]}. \quad (2)$$

The signal and idler photons were cleanly separated by a polarizing beam splitter (PBS) in our type-II SPDC configuration, so that the BFC was generated without post-selection. Using the temporal wavefunction, the BFC state can be rewritten as:

$$|\psi\rangle = \int dt e^{-\Delta\omega|\tau|} \sum_{m=-N_0}^{N_0} \text{sinc}(Am\Delta\Omega) \cos(m\Delta\Omega\tau) \hat{a}_H^\dagger(t) \hat{a}_V^\dagger(t+\tau) |0\rangle, \quad (3)$$

where we have used $\Delta\Omega/2\pi \ll B_{PM}$. The exponential decay in Eq. (3) is slowly varying relative to the $\sum_{m=-N_0}^{N_0} \text{sinc}(Am\Delta\Omega) \cos(m\Delta\Omega\tau)$ term because $\Delta\omega \ll \Delta\Omega$. Hence, the BFC's temporal wavefunction has many peaks, with repetition period equal to the cavity round-trip time, $\Delta T = 2\pi/\Delta\Omega$, where $\Delta T \approx 22.1$, 66.0 , and 198.8 ps for the BFCs generated by the 45.32, 15.15, and 5.03 GHz cavities, respectively.

A fiber Bragg grating (FBG) of 346 GHz bandwidth and a long-pass filter is used to spectrally select the BFC's $2N_0 + 1$ spectral modes in Eq. (1) and to filter out remaining pump photons. The BFC wavefunction in Eq. (3) implies that HOM-interference recurs at relative delays corresponding to integer multiples of the fiber cavity round-trip time^{35,63,64}, which we experimentally verified as follows. The orthogonally-polarized entangled photon pairs were divided by a PBS and directed to two arms of the HOM interferometer. A fiber polarization controller (FPC) in one arm of the interferometer alternates the idler photon polarization to match that of the signal photon at the 50:50 fiber coupler. A tunable free-space optical delay line with insertion loss smaller than 0.02 dB over its 220 mm travel range is used to vary the relative delay between the signal and idler photons for HOM-interference. After the HOM interferometer, coincidences are recorded with two superconducting nanowire single-photon detectors (SNSPDs, $\approx 85\%$ detection efficiency).

The HOM experimental results in Fig. 1b are measured with the 45.32 GHz FSR fiber cavity by scanning the relative optical delay between the biphotons from -340 to $+340$ ps with respect to the central dip. A pump power of 2 mW is chosen to avoid the multi-pair emissions that decrease two-photon interference visibility^{35,65}. The fringe visibility of the quantum interference, V_n for the n th dip is $[C_{\max} - C_{\min}(n)]/C_{\max}$, where C_{\max} is the maximum coincidence count and $C_{\min}(n)$ is the n th dip's minimum coincidence count. Figure 1b left inset zooms in on the central bin whose visibility is 98.4% before subtracting accidental coincidences, and 99.9% after they are subtracted. Here we note that the visibility of the central HOM dip must exceed 70.7% to be quantified as quantum biphoton interference⁶⁶ and, as the temporal delay between signal-idler increases from center dip, the HOM dips' visibilities decrease according to the fiber cavity's Lorentzian profile as described by the theory in Supplementary Discussion I. Moreover, we note that the variation of the central HOM dip's visibility between raw and subtracted data is small (1.5%), indicating that measurement noise is quite modest at the central HOM dip (edge dips are getting close to this noise limitation). The base-to-base width of the central dip—i.e., the relative optical delay difference between the left and right edges of the central HOM dip's triangular shape—is fitted to be 3.86 ± 0.30 ps, which agrees well with the reciprocal of our 245 GHz phase-matching bandwidth, as predicted by theory. We obtain HOM-interference recurrences for a total of 61 time bins within our setup optical delay scanning range, which is a significant advance over our prior studies³⁵. The measured repetition time of the recurrences was 11.03 ps, which corresponds to half the repetition period of the BFC⁶³, and agrees well with our theoretical

modeling in Supplementary Fig. 1. The visibility of the dip recurrences decreases exponentially (see Fig. 1b right inset) due to the Lorentzian lineshape of the BFC frequency bins. In particular, with the 45.32 GHz cavity's 11.03-ps bin spacing, our setup's ≈ 640 ps scan range allows us to observe 61 time bins given the visibility decay associated with that cavity's 1.56 GHz Lorentzian linewidth. A narrower linewidth and broader scan range would yield even more measurable time bins. Note that in addition to the HOM-interference recurrences, Franson interferometer and entanglement of formation is needed to help certify that we have generated the high-dimensionality BFC, as predicted by theory^{67,68}.

Frequency-bin correlations

Whereas HOM-interference recurrences arise from the periodic peaks in the BFC's time-domain wavefunction from Eq. (3), the BFC's frequency-bin correlations arise from the correlation structure inherent in its frequency-domain wavefunction from Eq. (1). Inasmuch as those wavefunctions comprise a Fourier-transform pair, we expect there will be time–frequency duality between HOM-interference recurrences and frequency-bin correlations, i.e., the more time bins there are the fewer frequency bins there will be and vice versa. To demonstrate that behavior, we measure spectral correlations between different signal-idler frequency-bin pairs. In the experiments presented in Fig. 2, we use either the 45.32 GHz FSR cavity or the 5.03 GHz FSR cavity. Each frequency-bin pairs are selected by a pair of tunable narrowband filters. For the 45.32 GHz cavity measurements in Fig. 2b, c, the filter has a 300 pm bandwidth; for the 5.03 GHz cavity results in Fig. 2d, the filter has a 100 pm bandwidth. In Fig. 2b, c, these frequency-bins range from -2 to $+2$, with 0 denoting frequency degeneracy. This figure shows that the BFC exhibits the energy-conservation and frequency correlation, based on Eq. (1). In addition, we investigate the impact of multi-pair emissions on the signal-idler frequency bin cross-talk, as shown in Fig. 2c. At ≈ 4 mW pump power, the strongest frequency-bin cross-talk increased by 5.4 to 6.31 dB compared to the ≈ 2 mW pump power case shown in Fig. 2b.

Figure 2d shows the greater number of BFC frequency bins obtained using the 5.03 GHz FSR cavity and 100 pm bandwidth tunable filters. In this measurement, although the temperature limit of these tunable filters ($\approx 100^\circ\text{C}$) limited the number of measurable frequency bins, there are now many more frequency bins compared to the case in Fig. 2b. We also note that higher signal-idler frequency-bin cross-talk is observed in the 5.03 GHz cavity due solely to the 100 pm bandwidth of our filter pairs, which spans several of that cavity's FSRs. We have measured and analyzed the frequency-bin (spectral-correlation) and time-bin (HOM-interference recurrence) subspaces for the BFCs we generated with the 5.03, 15.15³⁵, and 45.32 GHz cavities (measured HOM-interference recurrences for the 5.03 GHz cavity are shown in Supplementary Fig. 3). Theory tells us that the BFC's number of frequency bins N_Ω equals $2\pi B_{PM}/\Delta\Omega$, where $B_{PM} = 245$ GHz is the FWHM phase-matching bandwidth of the SPDC source, and its number of time bins N_T , within an inverse cavity linewidth, equals $\pi/\Delta\omega\Delta T$. Hence their product satisfies $N_T N_\Omega = \pi B_{PM}/\Delta\omega$ for all three cavities. For the ideal case, in which all the frequency bins are measurable, we find that

$$N_{T,45\text{ GHz}} N_{\Omega,45\text{ GHz}} \approx N_{T,15\text{ GHz}} N_{\Omega,15\text{ GHz}}. \quad (4)$$

where the subscripts label the cavity FSRs, owing to the nearly identical linewidths of the two cavities. In contrast, the time-bin and frequency-bin product for the 5.03 GHz cavity should be roughly a factor of three higher, owing to its smaller cavity linewidth. We note that this time-bin and frequency-bin tradeoff for any of our three cavities supports high-dimensional encoding for time–frequency QKD.

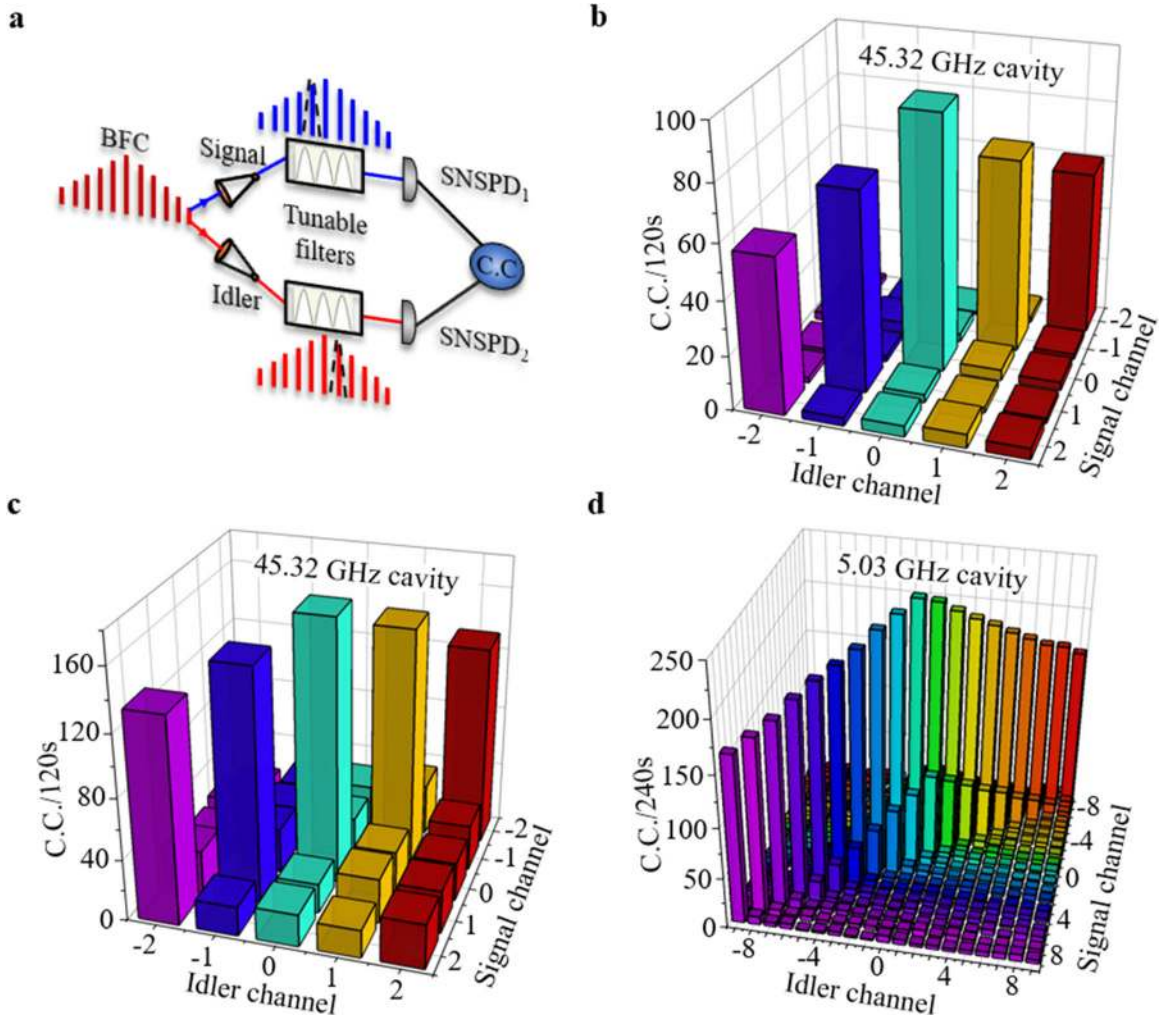


Fig. 2 Quantum frequency correlations of high-dimensional BFCs. **a** Experimental schematic for the joint spectral intensity measurement for the high-dimensional quantum state. Signal and idler photons are sent to two tunable narrowband filters for the frequency-bin correlation measurement with coincidence counting. **b** Measured frequency correlations of the 45.32 GHz BFC using filters that had matched FWHM bandwidths of 300 pm and were manually tuned for scans from the -2 to $+2$ frequency bins from frequency degeneracy. The SPDC source was pumped at ≈ 2 mW for these measurements, which produced relatively high coincidence counts only along the diagonal elements of the correlation matrix. The cross-talk between frequency bins was less than 11.71 dB. **c** Measured frequency correlations of the 45.32 GHz BFC when the SPDC crystal was pumped at ≈ 4 mW, showing increased signal-idler frequency-bin cross-talk to 6.31 dB. **d** Higher-dimensional frequency-bin joint spectral intensity measurements for the 5.03 GHz BFC. The filters used here had matched FWHM bandwidths of 100 pm and were temperature tuned for scans from the -9 to $+9$ frequency bins from frequency degeneracy. The off-diagonal components increase compared to those in Fig. 2a because the effective bandwidth of the tunable narrowband filters spanned multiple FSRs in this demonstration.

Post-selected polarization hyperentanglement measurement

The post-selected BFC state can be described by Eq. (1). Hence, we probe the polarization entanglement and frequency-polarization hyperentanglement by using the experimental setup in Fig. 3a. We couple the 45.32 GHz cavity BFC's outputs into low-loss fiber bench setups and performed the polarization entanglement measurement at the central HOM dip. The coupling loss for the fiber benches are ≈ 1.3 dB and ≈ 1.5 dB, respectively. We measured the post-selected polarization entanglement by recording the coincidence-count rates while changing the angle of polarizer P_2 when polarizer P_1 is set at 45° , 90° , 135° , and 180° . The results are shown in Fig. 3b, where we see that the measured fringes are well fit by sinusoidal curves, having accidentals-subtracted mean visibilities of $89.98 \pm 0.62\%$ [calculated using the $(C_{\max} - C_{\min}) / (C_{\max} + C_{\min})$ visibility definition for sinusoidal fringes]. Here we attribute the non-optimal polarization visibility to imperfect mode matching and limited PBS extinction ratio. Subsequently, by setting the optical delay at

0.7 mm, so that the signal and idler photons have a relative delay of ≈ 4.7 ps which is outside the central HOM dip (width = 3.86 ± 0.30 ps), we measured the polarization entanglement to demonstrate our BFC's post-selected frequency-polarization hyperentanglement. As shown in Fig. 3c, the measured fringes have accidentals-subtracted mean visibilities of $97.96 \pm 0.41\%$. The fitted results for Fig. 3c are used to obtain the correlation functions and the corresponding S parameters. The results are shown in Fig. 3d.

We measure the coincidences at the CHSH polarizer angles for the polarization subspace, and then calculate the S_{CHSH} parameter, which is given by⁶⁹:

$$S_{\text{CHSH}} = |E(\varphi_1, \varphi_2) - E(\varphi_1, \varphi'_2) + E(\varphi'_1, \varphi_2) + E(\varphi'_1, \varphi'_2)|, \quad (5)$$

where $E(\varphi_1, \varphi_2)$ is the two-photon correlation function at measurement angles of φ_1 and φ_2 , respectively. We choose to optimize S_{CHSH} by using $\varphi_1 = \pi/4$, $\varphi'_1 = \pi/2$, $\varphi_2 = 5\pi/8$, $\varphi'_2 = 7\pi/8$ ⁷⁰. We find S_{CHSH} to be 2.686 ± 0.037 from those

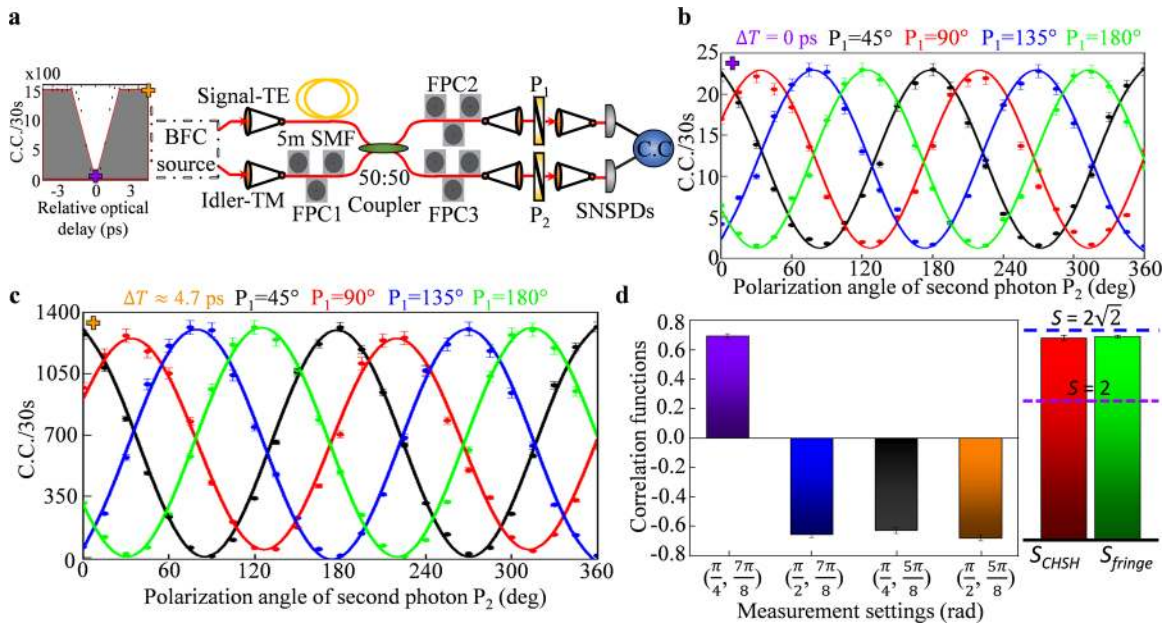


Fig. 3 Polarization hyperentanglement measurements of a high-dimensional 45.32 GHz BFC. **a** Illustrative experimental scheme in which the signal and idler photons from a 45.32 GHz BFC were sent to post-selected polarization entanglement measurements. The left inset of Fig. 1a is also included to indicate the frequency-polarization entanglement measurements after central HOM dip. The orange and purple marks indicate the position where the measurements are performed. P linear polarizer, C.C. coincidence counts. **b** Characterization of polarization entanglement at the central HOM dip with polarizer P_1 fixed at 45° (black curve), 90° (red curve), 135° (blue curve), and 180° (green curve). In all cases, we measured the coincidence-counting rates at the two outputs while changing polarizer P_2 from 0° to 360° . In all four cases the measured fringes are well fit with sinusoidal curves, having accidental-subtracted mean visibilities of $89.98 \pm 0.62\%$. **c** By setting the relative delay to 0.7 mm ($\approx 4.7 \text{ ps}$) away from the central HOM dip position, we measured the polarization entanglement of our BFC. The measured fringes have accidental-subtracted mean visibilities of $97.96 \pm 0.41\%$. **d** Correlation values needed for the CHSH inequality, performed for results in panel **c**. The abscissa label (φ_1, φ_2) denotes the measured polarization bases. The S_{CHSH} parameter was calculated to be 2.686 ± 0.037 from these correlations, which violates the CHSH inequality by 18.5 standard deviations. We obtained the maximal achievable S_{fringe} parameter to be 2.771 ± 0.016 from the mean visibility of the entanglement-correlation fringes. Purple and blue dashed lines denote the classical and quantum boundaries. Error bars represent statistical errors.

correlation values, which violates the CHSH inequality by 18.5 standard deviations. In addition, we estimate the maximum achievable S_{fringe} parameter of 2.771 ± 0.016 from the mean visibility of the entanglement-correlation fringes³⁰. The combination of post-selected polarization entanglement and HOM-interference is consistent with Eq. (1)'s implication that our BFC gives post-selected frequency-polarization hyperentanglement⁷¹.

Franson fringe recurrences and entanglement of formation

To further characterize and verify our BFC to support its being consistent—as predicted by theory—with high-quality time–frequency entanglement^{72–76}, we establish and stabilized a Franson interferometry which consists of two unbalanced Mach–Zehnder interferometers (MZIs), as shown in Fig. 4a. To achieve long-term stability, the MZIs are enclosed in a multilayer thermally-insulated enclosure whose temperature is actively stabilized. In Fig. 4a left inset the long-short path mismatch of each MZI is measured to be $\Delta T = 4.84 \text{ ns}$, which satisfies the requirement of phase-sensitive quantum fourth-order interference³⁵. We use a thermal heater in long path of arm1 to fine-tune the relative phase shift ΔT_1 between the two MZIs using our 45.32 GHz BFC. In addition, the motorized stage position ΔT_2 is fixed at the center of optimum Franson interference, with the maximum constructive interference shown in Fig. 4a left inset. A zoom-in shows the Franson interference visibility of up to 96.1% (99.1% after subtracting accidental coincidences) as shown in Fig. 4a right inset. Figure 4b shows the measured Franson interference fringes and that the recurrence period for them equals the fiber cavity round-trip time. The recurrences have a

22.09 ps period, and with fringe visibilities that decay according to the cavity Lorentzian lineshape as shown in Fig. 4c and in Supplementary Fig. 5. Moreover, when we move the motorized stage to a ΔT_2 in-between cavity round trips (non-integer) such as 33 ps, we indeed observe no fringes, as also shown in the inset of Fig. 4c. We note that we only measured for $\Delta T_2 \geq 0$, limited by the free-space optical delay line in the long path of arm2, which can reach up to 360 ps in our measurements.

To give quantitative lower bounds on the time-energy entanglement of our 45.32 GHz and 15.15 GHz BFCs, we calculate the entanglements of formation (E_{of})^{17,42,77} by using these state's Franson interference recurrences (zeroth- to the third-order for the 45.32 GHz and 15.15 GHz BFC). In Fig. 4d, we compute (E_{of}) up to 1.89 ± 0.03 ebits for the 45.32 GHz BFC and (E_{of}) up to 1.40 ± 0.05 ebits for the 15.15 GHz BFC. The theoretical E_{of} for visibilities V of 0.98 and 1 are also illustrated in the dashed line plots with 2 ebits as the maximum entanglement for a 4×4 high-dimensional biphoton. The close match between our results and ideal limits bolsters a nearly nonseparable BFC state generation. Detailed analysis numbers are also noted in Supplementary Table III.

Schmidt mode decompositions in the frequency and time domain

The BFC affords discrete-variable (binned) entanglement in both the frequency and time domains that can be quantified from our frequency-binned correlation measurements and our HOM-interference recurrences by means of Schmidt mode decompositions^{78,79} in the two domains. In both cases the relevant quantity

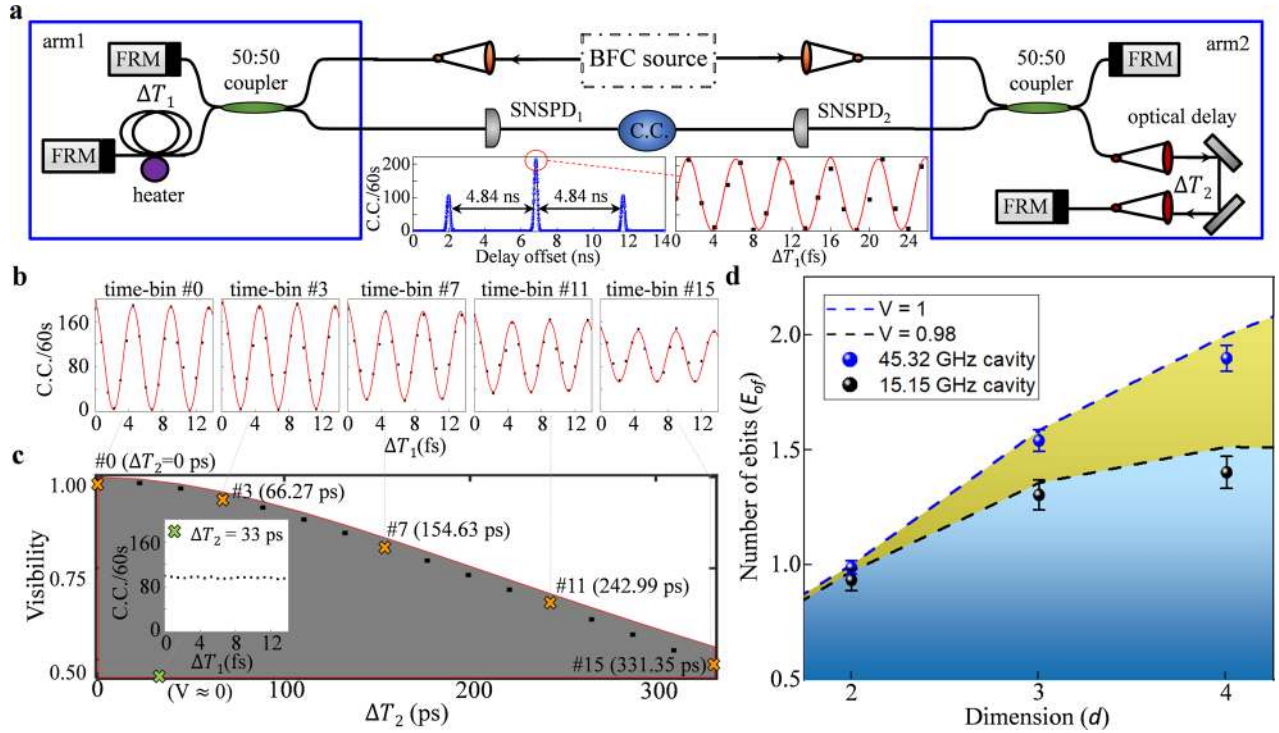


Fig. 4 Measured energy–time Franson revival interferometry of the high-dimensional biphoton frequency comb. **a** Experimental Franson interference setup. Faraday mirrors (FRMs) compensates the stress-birefringence of the single-mode fiber interferometers. A compact optical delay line is used in the longer path of arm2 (ΔT_2) to provide the tunability in optical delay up to 360 ps. Left inset: temporal two-photon waveforms (in blue) of Franson interferometry for constructive interferences. Right inset: zoom-in observed phase-sensitive interference fringe (in red) versus the relative optical delay introduced by the heater in long path of arm1 (ΔT_1). The observed Franson visibility is 96.1%, or 99.07% after subtracting the accidental coincidence counts. **b, c** Witnessed visibility of the Franson revival interference fringes. The coincidence counts in Franson interference experiments are selected for 0 (time-bin 0), 3, 7, 11, and 15 (time-bin 15) round-trip times of the 45.32 GHz fiber cavity (orange crosses; each round-trip time-bin at 22.09 ps), matching well with theoretical fringe envelope (red solid line; also further detailed in Supplementary Discussion II). Also included with the green cross in panel **c** inset is the Franson interference, when measured away from the integer time bins (such as at $\Delta T_2 = 33$ ps), with no observable interference fringes. **d** Lower bounds for the entanglement of formation (number of ebits) versus dimension d , in reconstructing the density matrix. Time–frequency entanglement containing up to 1.89 ± 0.03 ebits for the 45.32 GHz BFC out of the maximum 2 ebits when $d = 4$. For the 15.15 GHz BFC, the Franson interference recurrences extract 1.40 ± 0.05 ebits out of the maximum of 2 ebits (also detailed in Supplementary Discussion III).

is the Schmidt number K^{36} , defined as:

$$K = \left(\sum \lambda_n^2 \right)^{-1}, \text{ where } \sum \lambda_n = 1, \quad (6)$$

with $\{\lambda_n\}$ being the Schmidt mode eigenvalues.

For the frequency-binned case, the Schmidt eigenvalues are obtained from the frequency-binned joint spectral amplitude (JSA), $\psi(n_s \Delta \Omega, n_i \Delta \Omega)$ which can be obtained by discretizing the BFC's frequency-domain wavefunction $\psi(\omega_s, \omega_i)$, where ω_s and ω_i are the signal and idler detunings from frequency degeneracy. For ease of Schmidt-number analysis, we assume that our BFC is close to a pure state, based on the perturbation theory characterization of a cw-pumped SPDC and the excellent stabilization of our fiber Fabry–Pérot cavities. It is challenging, however, to measure the JSA because such measurements would require reconstruction of the full phase information of the entangled state. Instead, the joint spectral intensity (JSI) can be more readily measured by performing spectrally-resolved coincidence measurements, as shown in Fig. 2. Therefore, we will use our JSI data, viz., $|\psi(n_s \Delta \Omega, n_i \Delta \Omega)|^2$, and assume that the JSA satisfies

$$\psi(n_s \Delta \Omega, n_i \Delta \Omega) = \sqrt{|\psi(n_s \Delta \Omega, n_i \Delta \Omega)|^2}, \quad (7)$$

as predicted from perturbation theory with the signal-idler differential group delay suppressed. Then, by extracting the Schmidt eigenvalues $\{\lambda_n\}$ from the JSI measurements (i.e., the measured frequency-correlation matrix, such as Fig. 2d), the

Schmidt number of the frequency-binned state K_Ω , can be obtained as shown in Fig. 5a. This parameter indicates how many frequency-binned Schmidt modes are active in the biphoton state, and therefore describes its effective dimensionality³⁶. In particular, extracting the Schmidt eigenvalues $\{\lambda_n\}$ from the five resonance-pairs data of Fig. 2b for the 45.32 GHz FSR cavity and 2 mW pumping results in a frequency-bin Schmidt number $K_{\Omega, 45 \text{ GHz}} \approx 4.31$. For the 45.32 GHz FSR cavity with 4 mW pump power, the data in Fig. 2c leads to $K_{\Omega, 45 \text{ GHz}} \approx 3.17$, because the increased signal-idler frequency-bin cross-talk drops the purity of each diagonal frequency mode, resulting in a smaller Schmidt number. We also note that the increased multipair emissions responsible for this additional cross-talk makes the output of the BFC less like a biphoton. For our 15.15 GHz FSR cavity³⁵, we obtain a $K_{\Omega, 15 \text{ GHz}} \approx 8.67$ frequency-bin Schmidt number, where the number of frequency-correlated pairs is limited only by the maximum temperature tuning of our 100 pm FBG filters. Subsequently we used the frequency-bin data from Fig. 2d to find the 5.03 GHz cavity's frequency-bin Schmidt number. Using the third panel in Fig. 5a, we obtain $K_{\Omega, 5 \text{ GHz}} \approx 11.67$ for that cavity. This imperfect Schmidt number mostly due to the resolution bounds of our 100 pm bandwidth filters (the ideal Schmidt number for frequency-binned measurements is calculated in Supplementary Discussion IV), but it still demonstrates the scalability of our high-dimensional frequency-binned BFC. In Fig. 6a we compare the extracted frequency-bin Schmidt eigenvalues $\{\lambda_n\}$ for our three cavities (detailed calculations

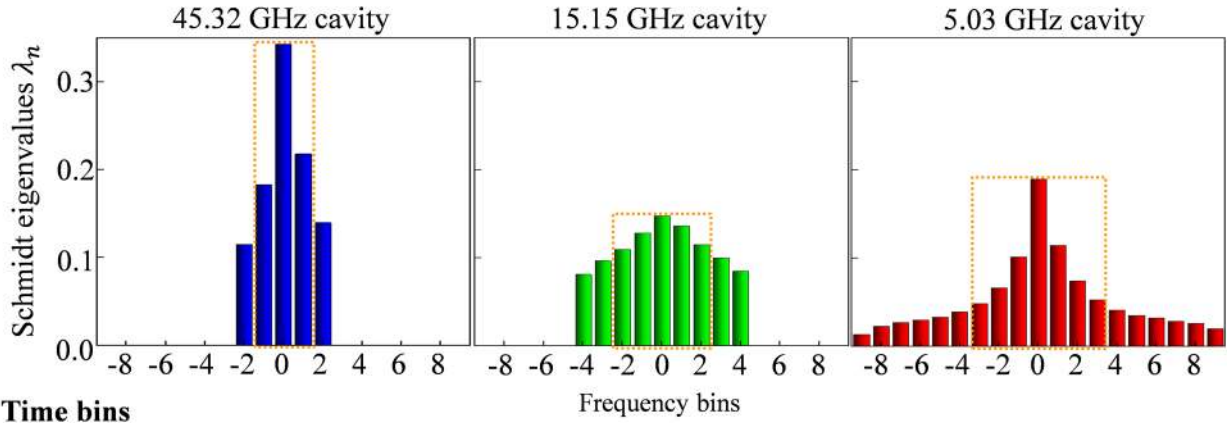
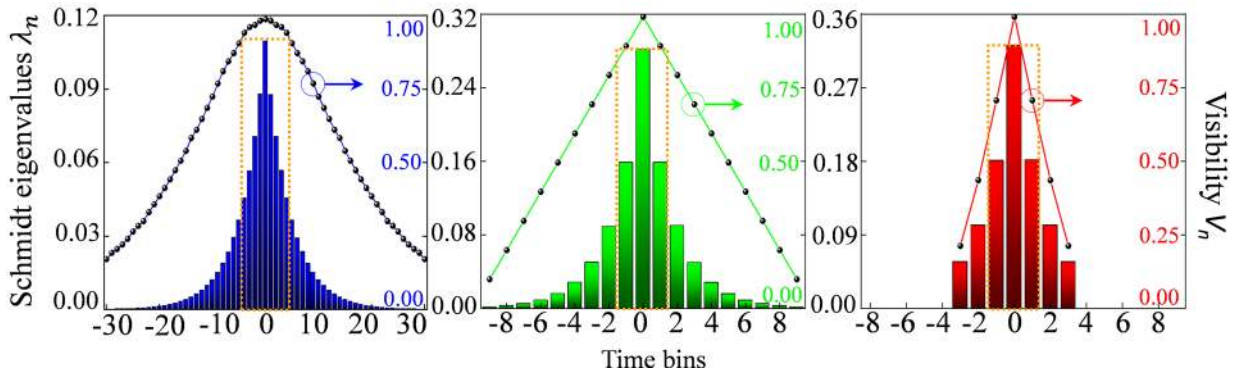
a Frequency bins**b Time bins**

Fig. 5 Schmidt mode decompositions for three high-dimensional BFCs. **a** The Schmidt mode eigenvalues for measured frequency-binned states obtained using our 45.32, 15.15, and 5.03 GHz FSR cavities with ≈ 2 mW pump power (calculation detailed in Supplementary Discussion IV). The obtained frequency-bin Schmidt numbers are $K_{\Omega,45 \text{ GHz}} \approx 4.31$, $K_{\Omega,15 \text{ GHz}} \approx 8.67$, and $K_{\Omega,5 \text{ GHz}} \approx 11.67$ for the three cavities. **b** The Schmidt mode eigenvalues versus different time bins from HOM interferometry and the corresponding visibilities of the HOM-interference recurrences. The blue, green, and red bars indicate the time-binned Schmidt eigenvalues for the 45.32, 15.15, and 5.03 GHz cavities, respectively, and the black points indicate the visibilities from HOM interferometry. The central HOM dip is labeled as 0 as a reference. The dominant Schmidt mode eigenvalues for each high-dimensional BFC have been highlighted under the orange-dashed boxes and detailed in Supplementary Discussion IV. The obtained time-bin Schmidt numbers are $K_{T,5 \text{ GHz}} \approx 5.16$, $K_{T,15 \text{ GHz}} \approx 6.71$, and $K_{T,45 \text{ GHz}} \approx 18.30$ for the three cavities.

of the Schmidt eigenvalues $\{\lambda_n\}$ and the resulting Schmidt numbers are in Supplementary Discussion IV).

Note that we obtain different frequency-binned BFC Schmidt numbers from the same SPDC phase-matching bandwidth by using cavities with different FSRs. From our measurements, the diagonal elements of the spectral-correlation matrix (Fig. 2d) show the decreasing-envelope behavior of the BFC. Hence, with the Schmidt decomposition, we have observed BFC states with Hilbert-space dimensionalities, $K_{\Omega} \times K_{\Omega}$, having lower bounds of at least 16 for the 45.32 GHz cavity, 64 for the 15.15 GHz cavity, and 121 for the 5.03 GHz cavity. Furthermore, the ideal full Hilbert-space dimensionalities are estimated to be at least $24 (= 4.9 \times 4.9)$ for the 45.32 GHz cavity, $400 (= 20 \times 20)$ for the 15.15 GHz cavity, and $1156 (= 34 \times 34)$ for the 5.03 GHz cavity, where the numbers arise from the detailed theory for the frequency-binned BFC's Schmidt number in Supplementary Discussion IV.

Turning now to the Schmidt number for the time-binned BFC, to proceed in a manner analogous to what we used for the frequency-binned BFC would require knowledge of the binned JTI. However, because our BFC is generated with cw pumping, this binned JTI—under the assumption of a pure-state biphoton—is a diagonal matrix with elements $|\psi(n\Delta T)|^2$, where $\psi(\tau)$ is the BFC's time-domain wavefunction from Eq. (3) and $n\Delta T$ is the relative delay between the signal and idler photons' n th time bin. We can estimate that binned JTI from our HOM-interference data, as we

now explain. By sampling $\psi(\tau)$ at $\tau = n\Delta T$, we get

$$|\psi(n\Delta T)|^2 = \frac{\exp(-2|n|\Delta\omega\Delta T)}{\sum_{n=-N_0}^{N_0} \exp(-2|n|\Delta\omega\Delta T)}, \quad (8)$$

for the JTI. From Supplementary Discussion I, we have that the visibility of the n th HOM dip is:

$$V_n = \exp(-|n|\Delta\omega\Delta T)(1 + |n|\Delta\omega\Delta T), \quad (9)$$

thus making it possible to find the BFC's JTI by inverting the one-to-one relation between $|n|\Delta\omega\Delta T$ and V_n . Measuring the binned joint-temporal amplitude (JTA), whose singular-value decomposition is the Schmidt decomposition, is prohibitively difficult. Hence, we assume, as predicted by Eq. (3), that it equals the square-root of the binned JTI, i.e., we use

$$\psi(n\Delta T) = \sqrt{|\psi(n\Delta T)|^2}, \quad (10)$$

for the time-binned wavefunction of the BFC, viz., its JTA, from which it follows that the time-bin Schmidt mode eigenvalues, $\{\lambda_n\}$, are given by:

$$\lambda_n = \frac{e^{-2n|n|/F}}{\sum_{n=-N}^N e^{-2n|n|/F}} = \frac{\sinh(\pi/F) \exp(-2n|n|/F)}{\cosh(\pi/F) - \exp(-(2N+1)\pi/F)}, \quad \text{for } 0 \leq |n| \leq N, \quad (11)$$

where $F = \Delta\Omega/2\Delta\omega$ is the cavity finesse. The time-binned BFC

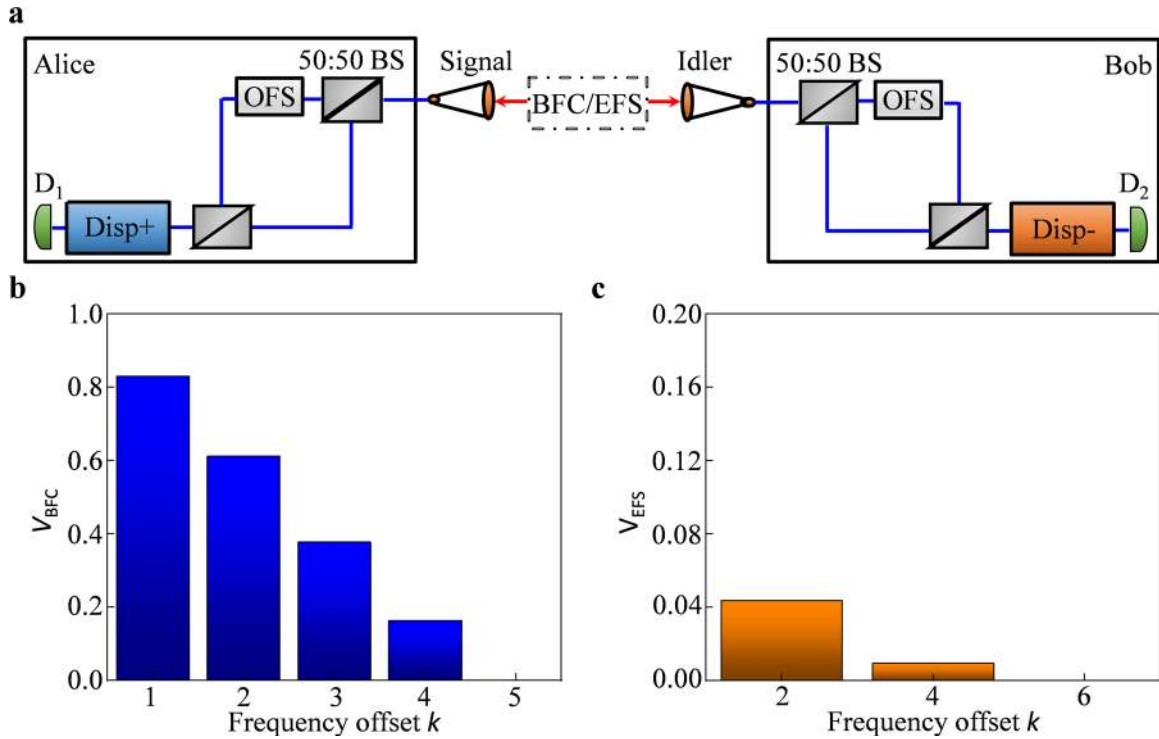


Fig. 6 Conjugate Franson interferometry and theoretical visibilities of conjugate Franson interference recurrences for the 45.32 GHz BFC and the EFS with the same JSI. **a** The proposed experimental setup for conjugate Franson interferometry. The signal and idler outputs from a filtered SPDC source are applied to a pair of MZIs. One arm of each MZI contains an OFS, i.e., a single-sideband modulator, that imposes frequency shifts $+\omega_m$ and $-\omega_m$ on the signal and idler, respectively. The MZI's outputs undergo positive (for the signal) and negative (for the idler) dispersions of equal magnitude that, together with the frequency shifts, ensure there is no second-order interference present in the signal-idler coincidence counts. **b** BFC theoretical conjugate Franson interference has high-visibility recurrences and they occur only when the interferometer frequency offset is $k\Delta\Omega$ for integer k . **c** EFS theoretical conjugate Franson interference has low-visibility recurrences and they only occur when the interferometer frequency offset is $2k\Delta\Omega$ for integer k . Supplementary Discussion V describes the details of conjugate Franson interferometry, comparing the BFC and EFS recurrence visibilities for the 15.15 GHz and 5.03 GHz cavities.

state's Schmidt number is then found from Eq. (6), which leads to the following theoretical results based on our three cavities' finesses: $K_{T,5 \text{ GHz}} \approx 5.16$, $K_{T,15 \text{ GHz}} \approx 6.71$, and $K_{T,45 \text{ GHz}} \approx 18.30$. By performing a parametric $(|n|\Delta\omega\Delta T)$ fit of our experimental data to the V_n expression in Eq. (9), and then applying the result in Eqs. (11) and (6), we obtain the experimental values $K_{T,5 \text{ GHz}} \approx 5.11$, $K_{T,15 \text{ GHz}} \approx 6.56$, and $K_{T,45 \text{ GHz}} \approx 18.02$, which agree well with theory. All the extracted time-binned Schmidt eigenvalues are shown in Fig. 5b.

For the 45.32 GHz cavity's BFC, the HOM-interference recurrences' lower bound on the Hilbert space dimensionality is therefore $K_{T,45 \text{ GHz}} \times K_{\Omega,45 \text{ GHz}} = 324$. Augmenting the time bins with the BFC's post-selected polarization entanglement doubles this dimensionality to at least 648. Furthermore, we find that the product of the time-binned and frequency-binned Schmidt numbers (when all the frequency bins are measurable, and the measurable HOM time bins run from -340 to 340 ps relative delay) is similar for the 45.32 GHz and 15.15 GHz BFCs:

$$K_{T,45 \text{ GHz}} K_{\Omega,45 \text{ GHz}} \cong K_{T,15 \text{ GHz}} K_{\Omega,15 \text{ GHz}}, \quad (12)$$

which mimics the BFC time–frequency product relation from Eq. (4).

Our Schmidt mode analysis demonstrates the effective time–frequency scaling (increase/decrease in number of bins) by using our BFCs. For the three fiber cavities that we measured, we have successfully scaled the time-binned Schmidt numbers from $K_{T,5 \text{ GHz}} \approx 5.11$ to $K_{T,45 \text{ GHz}} \approx 18.02$, limited by the finesses of the fiber cavities. In the frequency-binned subspace we scaled from $K_{\Omega,45 \text{ GHz}} \approx 4.31$ to $K_{\Omega,5 \text{ GHz}} \approx 11.67$, limited by the temperature tunability of the FBG filter. The scaling of time–frequency

dimensionality is complementary, the higher the Schmidt number in time or frequency, the smaller the Schmidt number in its conjugate domain. Multiplying the highest estimated time-binned Schmidt number by its frequency-binned Schmidt number counterpart yields a total Schmidt number of 77.67, which could encode over 12 qubits ($K_T K_\Omega \times K_T K_\Omega > 2^{12}$), with potentially 6.28 bits/photon [from $\log_2(K_T K_\Omega) = 6.28$] classical-information capacity that can be used in high-dimensional QKD.

Pure-state versus mixed state for filtered SPDC outputs

To this point we have asserted that our filtering of the signal and idler outputs from a cw-pumped SPDC source generates a nearly nonseparable-state BFC. Toward that end we have reported experimental results consistent with that interpretation: HOM-interference recurrences, frequency-bin correlations, Franson interference recurrences and their inferred entanglements of formation, and Schmidt mode decompositions in the time-bin and frequency-bin subspaces. Our BFC frequency-domain wavefunction's being an even function of detuning implies that its JSI determines its HOM-interference behavior⁶⁸, and in general the BFC's JSI determines its frequency-binned correlations and its Franson interference behavior (see Supplementary Discussion I, II, and V for details). That said, standard perturbation theory, see, e.g.,⁶², predicts that a cw-pumped SPDC will emit pure-state (or nearly pure-state) biphotons, and the excellent stabilization of our fiber Fabry–Pérot cavities then implies that our filtered SPDC sources should then emit nearly nonseparable-state BFC biphotons. Our prior experimental work supports the nearly pure-state assertion for a SPDC source's output, see⁸⁰, in which both the JSI and JTI were measured for a pulse-pumped

source, and⁸¹, in which an SPDC source was entanglement engineered to produce single spatiotemporal-mode heralded single-photon pulses. Moreover, we also note that there have been several experimental demonstrations of high-dimensional frequency-bin entanglement utilizing the sinusoidally driven phase modulator in recent years^{82–85}. Nevertheless, direct experimental evidence of a BFC state purity is highly desirable. Conjugate Franson interferometry³³, since it is characterized by the signal-idler state's JTI, can provide such evidence. The configuration for conjugate Franson interferometry is shown in Fig. 6a. Compared to our Franson interferometry setup in Fig. 4a, a pair of optical frequency shifters (OFSs) and dispersion modules are required to implement the conjugate Franson interferometry. In particular, this configuration easily allows the desired BFC pure state to be distinguished from mixed states with the same JSI. For example, Fig. 6b, c compare the visibilities for conjugate Franson interference recurrences of our 45.32 GHz BFC to those of the entangled frequency-pair state (EFS)—i.e., an incoherent mixture of the pure states,

$$|\psi_{\text{EFS}}^{(m)}\rangle = \int d\Omega f'(\Omega) [f(\Omega + m\Delta\Omega) + f(\Omega - m\Delta\Omega)] \hat{a}_H^\dagger\left(\frac{\omega_p}{2} + \Omega\right) \hat{a}_V^\dagger\left(\frac{\omega_p}{2} - \Omega\right) |0\rangle, \quad (13)$$

for $-N_0 \leq m \leq N_0$ —that has the same JSI (see Supplementary Discussion V for more details). The experimental implementation and stabilization of a conjugate Franson interferometer, challenging currently, can provide a pathway for future exploration of the high-dimensional BFC.

DISCUSSION

In this work we have demonstrated high-dimensionality time–frequency subspaces using a BFC generated by filtering the signal and idler outputs from a cw-pumped SPDC source. For a BFC generated with a 45.32 GHz FSR filter cavity we achieved 61 HOM-interference recurrences, with a maximum visibility of 98.4% (99.9%) before (after) accidental coincidences are subtracted. For a BFC generated with a 5.03 GHz FSR filter cavity, we observed high spectral correlations over 19 frequency bins. All told, for the three cavities we employed, we explored spectral and temporal correlations—and hence their Fourier-transform duality—over cavity FSRs spanning nearly an order of magnitude. We then measured up to 16 Franson interference recurrences, observing a maximum visibility of 96.0% (99.1%) before (after) accidental coincidences are subtracted. Using the zeroth to the third recurrence visibilities allowed us to obtain an $E_{\text{of}} \geq 1.89 \pm 0.03$ ebits—where 2 is the maximum for a 4×4 dimensional biphoton—lower bound on our BFC's entanglement. Via Schmidt mode decompositions, we quantified the entanglement scaling of our BFCs' time-binned and frequency-binned subspaces, comparing measured values with their theoretical counterparts. For example, our 45.32 GHz cavity's post-selected frequency-polarization hyperentangled BFC achieves a time-binned Schmidt number of 18 and a Hilbert-space dimensionality of at least 648, based on the assumption of a pure state, representing an advance of almost an order of magnitude compared to our previous work. With the time–frequency duality and the frequency-polarization hyperentanglement of such a BFC, we infer a computational space of more than 12 qubits, with 6.28 bits/photon that can potentially be encoded for classical-information transmission over a quantum channel using only biphotons. This high-dimensionality time–frequency state encodes multiple qubits from different degrees-of-freedom onto the biphoton pair, and thus further increasing the photon information capacity with applications in high-dimensional quantum information processing, time–frequency cluster-state quantum computation, and high-dimensional QKD.

METHODS

Experimental setups

For our cw-pumped source, we customized a tunable stabilized self-injection-locked 658 nm laser. We used a precision laser controller from Vescent Photonics (D2-105) to drive the laser diode. For other parts of experimental setups, we used the following components with all optical parts connected using either single-mode optical fibers or polarization-maintaining fibers: fiber-pigtailed ppKTP waveguide (AdvR), Fabry–Pérot fiber cavities (Luna/Micron Optics), bandpass filters (O/E Land and Agiltron), single-photon detectors (Photon Spot), and timing electronics (PicoQuant and Swabian Instruments).

Franson interferometry

For the phase-sensitive time-energy quantum interference measurements, we need to stabilize Franson interferometry to prevent the mechanical, acoustic, and thermal noises from the environment. Both MZI arms are shielded in double layers of sealed boxes, and temperature-stabilized with four home-made Peltier modules. The Franson interferometer free-space optical delay line (arm2, labeled in Fig. 4a) is based on a miniaturized linear stage with closed-loop piezoelectric motor control (CONEX-AG-LS25-27P, Newport). The optical insertion loss of double-pass free-space delay line is smaller than 0.4 ± 0.05 dB over the entire 360 ps delay-travel range, providing us the capability to measure Franson revival time bins from multiple cavities round-trip times of our BFC. For sub-femtosecond interference measurements, we utilize a temperature controller to thermally adjust the relative phase between the two arms of our Franson interferometer.

DATA AVAILABILITY

The data and analysis codes used in this study are available from the corresponding authors on request.

Received: 10 April 2020; Accepted: 12 February 2021;

Published online: 11 March 2021

REFERENCES

- Huang, Y.-F. et al. Experimental generation of an eight-photon Greenberger–Horne–Zeilinger state. *Nat. Commun.* **2**, 1–6 (2011).
- Chen, M., Menicucci, N. C. & Pfister, O. Experimental realization of multipartite entanglement of 60 modes of a quantum optical frequency comb. *Phys. Rev. Lett.* **112**, 120505 (2014).
- Debnath, S. et al. Demonstration of a small programmable quantum computer with atomic qubits. *Nature* **536**, 63–66 (2016).
- Malik, M. et al. Multi-photon entanglement in high dimensions. *Nat. Photonics* **10**, 248–252 (2016).
- Ding, D. S. et al. High-dimensional entanglement between distant atomic-ensemble memories. *Light Sci. Appl.* **5**, e16157 (2016).
- Bernien, H. et al. Probing many-body dynamics on a 51-atom quantum simulator. *Nature* **551**, 579–584 (2017).
- Zhang, J. et al. Observation of a many-body dynamical phase transition with a 53-qubit quantum simulator. *Nature* **551**, 601–604 (2017).
- Erhard, M., Malik, M., Krenn, M. & Zeilinger, A. Experimental Greenberger–Horne–Zeilinger entanglement beyond qubits. *Nat. Photonics* **12**, 759–764 (2018).
- Lu, H.-H. et al. Electro-optic frequency beam splitters and tritters for high-fidelity photonic quantum information processing. *Phys. Rev. Lett.* **120**, 030502 (2018).
- Arute, F. et al. Quantum supremacy using a programmable superconducting processor. *Nature* **574**, 505–510 (2019).
- X. Zhu. et al. Graph state engineering by phase modulation of the quantum optical frequency comb. Preprint at *arXiv* 1912.11215 (2019).
- Barreiro, J. T., Wei, T. C. & Kwiat, P. G. Beating the channel capacity limit for linear photonic superdense coding. *Nat. Phys.* **4**, 282–286 (2008).
- Krenn, M. et al. Generation and confirmation of a (100 × 100)-dimensional entangled quantum system. *Proc. Natl Acad. Sci. USA* **111**, 6243–6247 (2014).
- Anderson, B. E., Sosa-Martinez, H., Ríofrío, C. A., Deutsch, Ivan H. & Jessen, P. S. Accurate and robust unitary transformations of a high-dimensional quantum system. *Phys. Rev. Lett.* **114**, 240401 (2015).
- Kumar, K. S., Vepsäläinen, A., Danilin, S. & Paraoanu, G. S. Stimulated Raman adiabatic passage in a three-level superconducting circuit. *Nat. Commun.* **7**, 1–6 (2016).

16. Manurkar, P. et al. Multidimensional mode-separable frequency conversion for high-speed quantum communication. *Optica* **3**, 1300–1307 (2016).
17. Martin, A. et al. Quantifying photonic high-dimensional entanglement. *Phys. Rev. Lett.* **118**, 110501 (2017).
18. Wang, J. et al. Multidimensional quantum entanglement with large-scale integrated optics. *Science* **360**, 285–291 (2018).
19. Kues, M. et al. Quantum optical microcombs. *Nat. Photonics* **13**, 170–179 (2019).
20. Erhard, M., Krenn, M. & Zeilinger, A. Advances in high-dimensional quantum entanglement. *Nat. Rev. Phys.* **2**, 365–381 (2020).
21. Lloyd, S., Shapiro, J. H. & Wong, F. N. C. Quantum magic bullets by means of entanglement. *J. Opt. Soc. Am. B* **19**, 312–318 (2002).
22. Dada, A. C., Leach, J., Buller, G. S., Padgett, M. J. & Andersson, E. Experimental high-dimensional two-photon entanglement and violations of generalized Bell inequalities. *Nat. Phys.* **7**, 677–680 (2011).
23. Kulkarni, G., Sahu, R., Magaña-Loaiza, O. S., Boyd, R. W. & Jha, A. K. Single-shot measurement of the orbital-angular-momentum spectrum of light. *Nat. Commun.* **8**, 1–8 (2017).
24. Howland, G. A., Knarr, S. H., Schneeloch, J., Lum, D. J. & Howell, J. C. Compressively characterizing high-dimensional entangled states with complementary, random filtering. *Phys. Rev. X* **6**, 021018 (2016).
25. Aguilar, E. A. et al. Certifying an irreducible 1024-dimensional photonic state using refined dimension witnesses. *Phys. Rev. Lett.* **120**, 230503 (2018).
26. Wang, J., Sciarrino, F., Laing, A. & Thompson, M. G. Integrated photonic quantum technologies. *Nat. Photonics* **14**, 273–284 (2020).
27. Schneeloch, J., Tison, C. C., Fanto, M. L., Alsing, P. M. & Howland, G. A. Quantifying entanglement in a 68-billion-dimensional quantum state space. *Nat. Commun.* **10**, 1–7 (2019).
28. Cariñe, J. et al. Multi-core fiber integrated multi-port beam splitters for quantum information processing. *Optica* **7**, 542–550 (2020).
29. Cheng, X. et al. An efficient on-chip single-photon SWAP gate for entanglement manipulation. In *Conference on Lasers and Electro-Optics*, paper FM2R.5 (OSA Technical Digest, Optical Society of America, 2020).
30. Wang, J. et al. Chip-to-chip quantum photonic interconnect by path-polarization interconversion. *Optica* **3**, 407–413 (2016).
31. Wengerowsky, S., Joshi, S. K., Steinlechner, F., Hübel, H. & Ursin, R. An entanglement-based wavelength-multiplexed quantum communication network. *Nature* **564**, 225–228 (2018).
32. Shalm, L. K. et al. Three-photon energy-time entanglement. *Nat. Phys.* **9**, 19–22 (2013).
33. Zhang, Z., Mower, J., Englund, D., Wong, F. N. C. & Shapiro, J. H. Unconditional security of time-energy entanglement quantum key distribution using dual-basis interferometry. *Phys. Rev. Lett.* **112**, 120506 (2014).
34. Zhong, T. et al. Photon-efficient quantum key distribution using time–energy entanglement with high-dimensional encoding. *N. J. Phys.* **17**, 022002 (2015).
35. Xie, Z. et al. Harnessing high-dimensional hyperentanglement through a biphoton frequency comb. *Nat. Photonics* **9**, 536–542 (2015).
36. Kues, M. et al. On-chip generation of high-dimensional entangled quantum states and their coherent control. *Nature* **546**, 622–626 (2017).
37. Rödiger, J. et al. Numerical assessment and optimization of discrete-variable time-frequency quantum key distribution. *Phys. Rev. A* **95**, 052312 (2017).
38. Lu, H.-H. et al. Quantum interference and correlation control of frequency-bin qubits. *Optica* **5**, 1455–1460 (2018).
39. Jaramillo-Villegas, J. A. et al. Persistent energy–time entanglement covering multiple resonances of an on-chip biphoton frequency comb. *Optica* **4**, 655–658 (2017).
40. Davis, A. O., Thiel, V. & Smith, B. J. Measuring the quantum state of a photon pair entangled in frequency and time. *Optica* **7**, 1317–1322 (2020).
41. Chang, K.-C. et al. High-dimensional energy-time entanglement up to 6 qubits per photon through biphoton frequency comb. In *Conference on Lasers and Electro-Optics*, paper JTu3A.6 (OSA Technical Digest, Optical Society of America, 2019).
42. Imany, P. et al. High-dimensional optical quantum logic in large operational spaces. *npj Quantum Inf.* **5**, 59 (2019).
43. Chang, K.-C. et al. High-dimensional time-frequency entanglement and Schmidt number witnesses using a biphoton frequency comb. In *Conference on Lasers and Electro-Optics*, paper JTh2A.23 (OSA Technical Digest, Optical Society of America, 2020).
44. Lu, H. H. et al. Quantum phase estimation with time-frequency qudits in a single photon. *Adv. Quantum Technol.* **3**, 1900074 (2020).
45. Reimer, C. et al. High-dimensional one-way quantum processing implemented on d -level cluster states. *Nat. Phys.* **15**, 148–153 (2018).
46. Steinlechner, F. et al. Distribution of high-dimensional entanglement via an intracity free-space link. *Nat. Commun.* **8**, 15971 (2017).
47. Ding, Y. et al. High-dimensional quantum key distribution based on multicore fiber using silicon photonic integrated circuits. *npj Quantum Inf.* **3**, 1–7 (2017).
48. Khan, I. A., Broadbent, C. J. & Howell, J. C. Large-alphabet quantum key distribution using energy-time entangled bipartite states. *Phys. Rev. Lett.* **98**, 060503 (2007).
49. Chapman, J. C., Lim, C. C. & Kwiat, P. G. Hyperentangled time-bin and polarization quantum key distribution. Preprint at *arXiv* 1908.09018 (2019).
50. Chapman, J. C., Graham, T. M., Zeilinger, C. K., Bernstein, H. J. & Kwiat, P. G. Time-bin and polarization superdense teleportation for space applications. *Phys. Rev. Appl.* **14**, 014044 (2020).
51. Huber, M. & Pawłowski, M. Weak randomness in device-independent quantum key distribution and the advantage of using high-dimensional entanglement. *Phys. Rev. A* **88**, 032309 (2013).
52. Horodecki, R., Horodecki, P., Horodecki, M. & Horodecki, K. Quantum entanglement. *Rev. Mod. Phys.* **81**, 865 (2009).
53. Ecker, S. et al. Overcoming noise in entanglement distribution. *Phys. Rev. X* **9**, 041042 (2019).
54. Collins, D., Gisin, N., Linden, N., Massar, S. & Popescu, S. Bell inequalities for arbitrarily high-dimensional systems. *Phys. Rev. Lett.* **88**, 040404 (2002).
55. Thew, R. T., Acín, A., Zbinden, H. & Gisin, N. Bell-type test of energy-time entangled qutrits. *Phys. Rev. Lett.* **93**, 010503 (2004).
56. Reimer, C. et al. Generation of multiphoton entangled quantum states by means of integrated frequency combs. *Science* **351**, 1176–1180 (2016).
57. Bavaresco, J. et al. Measurements in two bases are sufficient for certifying high-dimensional entanglement. *Nat. Phys.* **14**, 1032–1037 (2018).
58. Rambach, M. et al. Hectometer revivals of quantum interference. *Phys. Rev. Lett.* **121**, 093603 (2018).
59. Brańczyk, A.M. Hong-ou-mandel interference. Preprint at *arXiv* 1711.00080 (2017).
60. Zhong, T., Wong, F. N. C., Roberts, T. D. & Battle, P. High performance photon-pair source based on a fiber-coupled periodically poled KTiOPO4 waveguide. *Opt. Express* **17**, 12019–12030 (2009).
61. Zhong, T. et al. High-quality fiber-optic polarization entanglement distribution at 1.3 μm telecom wavelength. *Opt. Lett.* **35**, 1392–1394 (2010).
62. Giovannetti, V., Maccone, L., Shapiro, J. H. & Wong, F. N. C. Generating entangled two-photon states with coincident frequencies. *Phys. Rev. Lett.* **88**, 183602 (2002).
63. Lu, Y. J., Campbell, R. L. & Ou, Z. Y. Mode-locked two-photon states. *Phys. Rev. Lett.* **91**, 163602 (2003).
64. Shapiro, J.H. Coincidence dips and revivals from a type-II optical parametric amplifier. In *Technical Digest of Topical Conference on Nonlinear Optics*, paper FC7-1 (Maui, HI, 2002).
65. Xu, X. et al. Near-infrared Hong-Ou-Mandel interference on a silicon quantum photonic chip. *Opt. Express* **21**, 5014–5024 (2013).
66. Rarity, J. G. & Tapster, P. R. Experimental violation of Bell's inequality based on phase and momentum. *Phys. Rev. Lett.* **64**, 2495 (1990).
67. Jin, R. B. & Shimizu, R. Extended Wiener–Khinchin theorem for quantum spectral analysis. *Optica* **5**, 93–98 (2018).
68. Lingaraju, N. B. et al. Quantum frequency combs and Hong-Ou-Mandel interferometry: the role of spectral phase coherence. *Opt. Express* **27**, 38683–38697 (2019).
69. Clauser, J. F., Horne, M. A., Shimony, A. & Holt, R. A. Proposed experiment to test local hidden-variable theories. *Phys. Rev. Lett.* **23**, 880 (1969).
70. Kuzucu, O. & Wong, F. N. C. Pulsed Sagnac source of narrow-band polarization-entangled photons. *Phys. Rev. A* **77**, 032314 (2008).
71. Chen, Y. et al. Verification of high-dimensional entanglement generated in quantum interference. *Phys. Rev. A* **101**, 032302 (2020).
72. Franson, J. D. Bell inequality for position and time. *Phys. Rev. Lett.* **62**, 2205 (1989).
73. Kutluer, K. et al. Time entanglement between a photon and a spin wave in a multimode solid-state quantum memory. *Phys. Rev. Lett.* **123**, 030501 (2019).
74. Coles, P. J., Katarinya, V., Lloyd, S., Marvian, I. & Wilde, M. M. Entropic energy-time uncertainty relation. *Phys. Rev. Lett.* **122**, 100401 (2019).
75. Oser, D. et al. High-quality photonic entanglement out of a stand-alone silicon chip. *npj Quantum Inf.* **6**, 1–6 (2020).
76. Zhao, J., Ma, C., Rüsing, M. & Mookherjee, S. High quality entangled photon pair generation in periodically poled thin-film lithium niobate waveguides. *Phys. Rev. Lett.* **124**, 163603 (2020).
77. Tiranov, A. et al. Quantification of multidimensional entanglement stored in a crystal. *Phys. Rev. A* **96**, 040303 (2017).
78. Francis-Jones, R. J., Hoggarth, R. A. & Mosley, P. J. All-fiber multiplexed source of high-purity single photons. *Optica* **3**, 1270–1273 (2016).
79. Zielenicki, K. et al. Joint spectral characterization of photon-pair sources. *J. Mod. Opt.* **65**, 1141–1160 (2018).
80. Kuzucu, O., Wong, F. N. C., Kurimura, S. & Tovstonog, S. Joint temporal density measurements for two-photon state characterization. *Phys. Rev. Lett.* **101**, 153602 (2008).
81. Chen, C. et al. Indistinguishable single-mode photons from spectrally-engineered biphotons. *Opt. Express* **27**, 11626–11634 (2019).
82. Sensarn, S., Yin, G. Y. & Harris, S. E. Observation of nonlocal modulation with entangled photons. *Phys. Rev. Lett.* **103**, 163601 (2009).
83. Imany, P. et al. 50-GHz-spaced comb of high-dimensional frequency-bin entangled photons from an on-chip silicon nitride microresonator. *Opt. Express* **26**, 1825–1840 (2018).

84. Imany, P., Odele, O. D., Jaramillo-Villegas, J. A., Leaird, D. E. & Weiner, A. M. Characterization of coherent quantum frequency combs using electro-optic phase modulation. *Phys. Rev. A* **97**, 013813 (2018).
85. Imany, P., Lingaraju, N. B., Alshaykh, M. S., Leaird, D. E. & Weiner, A. M. Probing quantum walks through coherent control of high-dimensionally entangled photons. *Sci. Adv.* **6**, eaba8066 (2020).

ACKNOWLEDGEMENTS

The authors acknowledge discussions with Pengfei Fan, Changchen Chen, Wei Liu, Jiahui Huang, Andrei Faraon, Patrick Hayden, Mi Lei, Maria Spiropulu, Charles Ci Wen Lim, Alexander Euk Jin Ling, and discussions on the superconducting single-photon detectors with Vikas Anant, Matthew Shaw, and Boris Korzh. This study was supported by the National Science Foundation under award numbers 1741707 (EFRI ACQUIRE), 1919355, and 1936375 (QII-TAQS).

AUTHOR CONTRIBUTIONS

K.-C.C. and X.C. lead the project and contributed equally. K.-C.C. and X.C. performed the measurements and data analysis. M.C.S., A.K.V., and Y.S.L. contributed to the measurements. J.H.S., K.-C.C., and Y.X.G. contributed to the theory and numerical modeling sections. T.Z., Z.X., F.N.C.W., and C.W.W. supported and discussed the studies. K.-C.C., J.H.S., F.N.C.W., and C.W.W. prepared the manuscript. All authors contributed to the discussion and revision of the manuscript.

COMPETING INTERESTS

The authors declare no competing interests.

ADDITIONAL INFORMATION

Supplementary information The online version contains supplementary material available at <https://doi.org/10.1038/s41534-021-00388-0>.

Correspondence and requests for materials should be addressed to K.-C.C., X.C., Z.X. or C.W.W.

Reprints and permission information is available at <http://www.nature.com/reprints>

Publisher's note Springer Nature remains neutral with regard to jurisdictional claims in published maps and institutional affiliations.



Open Access This article is licensed under a Creative Commons Attribution 4.0 International License, which permits use, sharing, adaptation, distribution and reproduction in any medium or format, as long as you give appropriate credit to the original author(s) and the source, provide a link to the Creative Commons license, and indicate if changes were made. The images or other third party material in this article are included in the article's Creative Commons license, unless indicated otherwise in a credit line to the material. If material is not included in the article's Creative Commons license and your intended use is not permitted by statutory regulation or exceeds the permitted use, you will need to obtain permission directly from the copyright holder. To view a copy of this license, visit <http://creativecommons.org/licenses/by/4.0/>.

© The Author(s) 2021